How to cite: *Angew. Chem. Int. Ed.* **2025**, *64*, e202504641
doi.org/10.1002/anie.202504641

Ammonia Electrosynthesis

Enhanced *p–d* Orbital Coupling in Unconventional Phase RhSb Alloy Nanoflowers for Efficient Ammonia Electrosynthesis in Neutral Media

Fu Liu[+], Jingwen Zhou[+], Mingzi Sun[+], Zhihang Xu[+], Helin Wang, Ning Yao, Yunhao Wang, Fengkun Hao, Yuecheng Xiong, Juan Wang, Liang Guo, Qingbo Wa, Guozhi Wang, Xiang Meng, Mingzheng Shao, Chaohui Wang, Hsiao-Chien Chen, Hao Ming Chen, Ye Zhu,* Bolong Huang,* and Zhanxi Fan**

Abstract: Phase control provides a promising approach for physicochemical property modulation of metal/alloy nanomaterials toward various electrocatalytic applications. However, the controlled synthesis of alloy nanomaterials with unconventional phases remains challenging, especially for those containing both *p*- and *d*-block metals. Here, we report the one-pot synthesis of ultrathin RhSb alloy nanoflowers (NFs) with an unconventional 2H phase. Using 2H RhSb NFs as an electrocatalyst for nitrite reduction reaction in neutral media, the optimal NH_3 Faradaic efficiency and yield rate can reach up to 96.8% and 47.2 mg h^{-1} mg_{cat}^{-1} at −0.3 and −0.6 V (vs. reversible hydrogen electrode), respectively. With 2H RhSb NFs as a bifunctional cathode catalyst, the as-assembled zinc-nitrite/methanol batteries deliver a high energy efficiency of 96.4% and improved rechargeability with 120-h stable running. Ex/in situ characterizations and theoretical calculations have demonstrated that the phase change of RhSb from face-centered cubic (*fcc*) to 2H has optimized the electronic structure through stronger interactions between Rh and Sb by *p–d* orbital couplings, which improves the adsorption of key intermediates and reduces the reaction barriers of nitrite reduction to guarantee the efficient electrocatalysis. This work offers a feasible strategy of boosting the electrocatalytic performance of alloy nanostructures by integrating phase control and *p–d* orbital coupling.

[*] F. Liu[+], J. Zhou[+], M. Sun[+], Y. Wang, F. Hao, Y. Xiong, J. Wang, L. Guo, Q. Wa, G. Wang, X. Meng, M. Shao, C. Wang, B. Huang, Z. Fan
Department of Chemistry, City University of Hong Kong, Kowloon, Hong Kong SAR 999077, China
E-mail: b.h@cityu.edu.hk
zhanxi.fan@cityu.edu.hk

J. Zhou[+], Y. Wang, Y. Xiong, L. Guo, G. Wang, X. Meng, M. Shao, Z. Fan
Hong Kong Branch of National Precious Metals Material Engineering Research Center (NPMM), City University of Hong Kong, Kowloon, Hong Kong SAR 999077, China

Z. Xu[+], Y. Zhu
Department of Applied Physics, Research Institute for Smart Energy, The Hong Kong Polytechnic University, Kowloon, Hong Kong SAR 999077, China
E-mail: yezhu@polyu.edu.hk

H. M. Chen
Department of Chemistry, National Taiwan University, Taipei 10617, Taiwan

H.-C. Chen
Center for Reliability Science and Technologies, Chang Gung University, Taoyuan 333323, Taiwan
E-mail: hc_chen@mail.cgu.edu.tw

H. Wang
Hubei Key Laboratory of Energy Storage and Power Battery, School of Mathematics, Physics and Optoelectronic Engineering, Hubei University of Automotive Technology, Shiyan 442002, China

N. Yao
State Key Laboratory of Solidification Processing, Center for Nano Energy Materials, School of Materials Science and Engineering, Shaanxi Joint Laboratory of Graphene, Northwestern Polytechnical University, Xi'an 710072, China

Z. Fan
Hong Kong Institute for Clean Energy, City University of Hong Kong, Kowloon, Hong Kong SAR 999077, China

Z. Fan
City University of Hong Kong Shenzhen Research Institute, Shenzhen 518057, China

M. Sun[+], B. Huang
Department of Applied Biology and Chemical Technology, The Hong Kong Polytechnic University, Kowloon, Hong Kong SAR 999077, China

[+] These authors contributed equally to this work.

Additional supporting information can be found online in the Supporting Information section

Introduction

The excess production and accumulation of "active" nitrogen species have led to a severe imbalance of the global nitrogen cycle, further triggering a series of environmental concerns that threaten the survival of humanity.[1–4] As a key intermediate of the nitrogen cycle, nitrite (NO_2^-) is categorized as a Group 2A carcinogen by the World Health Organization, which can bind to the hemoglobin and cause some virulent diseases (e.g., blue baby syndrome and cancer).[5–7] Unfortunately, NO_2^- is widely found in industrial effluent, groundwater, and even natural water bodies with nonnegligible hazards.[8–11] Therefore, it's of great significance to conduct the efficient and sustainable conversion of pernicious NO_2^- into green and value-added products so as to achieve a win–win situation for both environmental protection and economic development.

Electrocatalytic NO_2^- reduction reaction (NO_2RR) to ammonia (NH_3) provides a promising paradigm in which NH_3 is an essential carrier for both agriculture and industry.[12–14] As a multistep hydrogenation process, NO_2RR involves the seven-proton and six-electron transfer with various intermediates (e.g., NO*, NHO*, N*, NHOH*, NH_2OH*, and NH*). In particular, the combination of H with these nitrogenous intermediates and the affinity between H and H atoms for coupling will affect the final product distribution.[15–18] As a critical indicator dominating the NO_2RR performance, the surface adsorption behavior of active hydrogen (H*) is largely affected by both the electrolyte environment and catalyst material. In practical scenarios, it's critical to maintain the normal operation of catalyst in the effluent of neutral media given that adding a pH regulator will inevitably compromise the target cost-profit relationship in the industrialized treatment.[19–22] To optimize the H* adsorption and suppress the competitive hydrogen evolution reaction (HER) upon NO_2RR in neutral electrolytes, some strategies for metal-based materials have been developed to tune the electronic structure of catalysts and tailor the adsorption energy of intermediates, e.g., interface/surface modification, defect construction, and heterojunction design.[13,16,23–29] However, the catalytic property of metal-based materials is largely determined by their intrinsic structure, i.e., the mode of atomic arrangement.[30–35] Meanwhile, the quantity of active sites of catalysts is largely determined by their size and morphology, the regulation of which is consequently essential to boost the NH_3 yield rate.[36–40] Based on this issue, the developed nanostructure modulation and atomic-level dispersion (e.g., single-atom construction) strategies can improve the atomic utilization efficiency to some degree, but the applied voltage and final Faradaic efficiency (FE) of NH_3 mostly show a compensatory relationship.[25,41–44] Therefore, the prominent regulation on the intrinsic property of catalysts toward efficient nitrite conversion with low energy consumption is yet to be achieved, especially in the neutral environment.

Crystal phase, essentially defining the atomic arrangement pattern, largely affects the physicochemical properties of nanomaterials. Theoretically, most materials can display two or more kinds of crystal phases by diverse atomic packing modes, while their conventional phase is only one, which is the most thermodynamically stable from energetic perspective.[33,45–47] In comparison, the unconventional phases rarely exist in nature in most cases due to their thermodynamically unstable peculiarity. However, this provides a great opportunity to artificially synthesize the unconventional phases and further study their elusive properties/performances. Therefore, crystal phase control of nanomaterials has attracted enormous attention with rapid development for the application attempt in various fields.[45,48,49] In the specific redox reactions for electrosynthesis, some critical intermediates can be preferentially generated by energy level regulation.[35,50–52] In this regard, the phase control of metal-based catalysts on NO_2RR can offer an efficient approach for target modification of hydrogenation/deoxygenation activities. Moreover, benefitting from the unique valence electrons in p orbitals, the *p*-block metals can alloy with *d*-block metals for the intermediate adsorption/desorption regulation upon NO_2RR, in which the electronic interactions can be significantly improved by *p–d* orbital hybridization.[53–55] However, the controlled synthesis of unconventional phase alloy nanomaterials containing both *p*- and *d*-block metals remains challenging.

In this work, the rhodium–antimony (RhSb) alloy nanoflowers (NFs) with unconventional 2H phase were synthesized via a facile one-pot method. Compared with the counterparts of face-centered cubic (*fcc*)-phase RhSb nanodendrites (NDs) and 2H-phase Rh NFs, 2H RhSb NFs exhibited much superior NO_2RR activity and selectivity in neutral medium for NH_3 synthesis, the optimal FE and yield rate of which can reach up to 96.8% and 47.2 mg h^{-1} mg_{cat}^{-1} at −0.3 and −0.6 V (vs. RHE), respectively. Impressively, the as-constructed zinc-nitrite/methanol (Zn-NO_2^-/MeOH) batteries using 2H RhSb NFs cathode could deliver an ultrahigh energy efficiency of 96.4%, remarkable rate capability, and well cycling stability for 120 h. Ex/in situ experimental characterizations and density functional theory (DFT) calculations have investigated the electronic modulations for 2H and fcc RhSb models, where the *p–d* orbital couplings are enhanced in 2H RhSb with the upshifted *d*-band center of Rh-4*d* orbitals toward faster electron transportations. Accordingly, 2H RhSb displays efficient proton generation to realize the stronger reaction trends of NO_2RR. Such joint alloying and phase engineering strategy could be regarded as a general paradigm to modulate the adsorption of intermediates in various electrocatalytic reactions, enabling more promising applications of hybrid energy system.

Results and Discussion

Synthesis and Characterization

The synthetic processes of 2H-phase RhSb NFs and *fcc*-phase RhSb NDs are schematically illustrated in Figure 1a (see more details in Supporting Information). Specifically, the nucleation kinetics of RhSb nanoalloy can be regulated by using different reductants and capping agents, finally

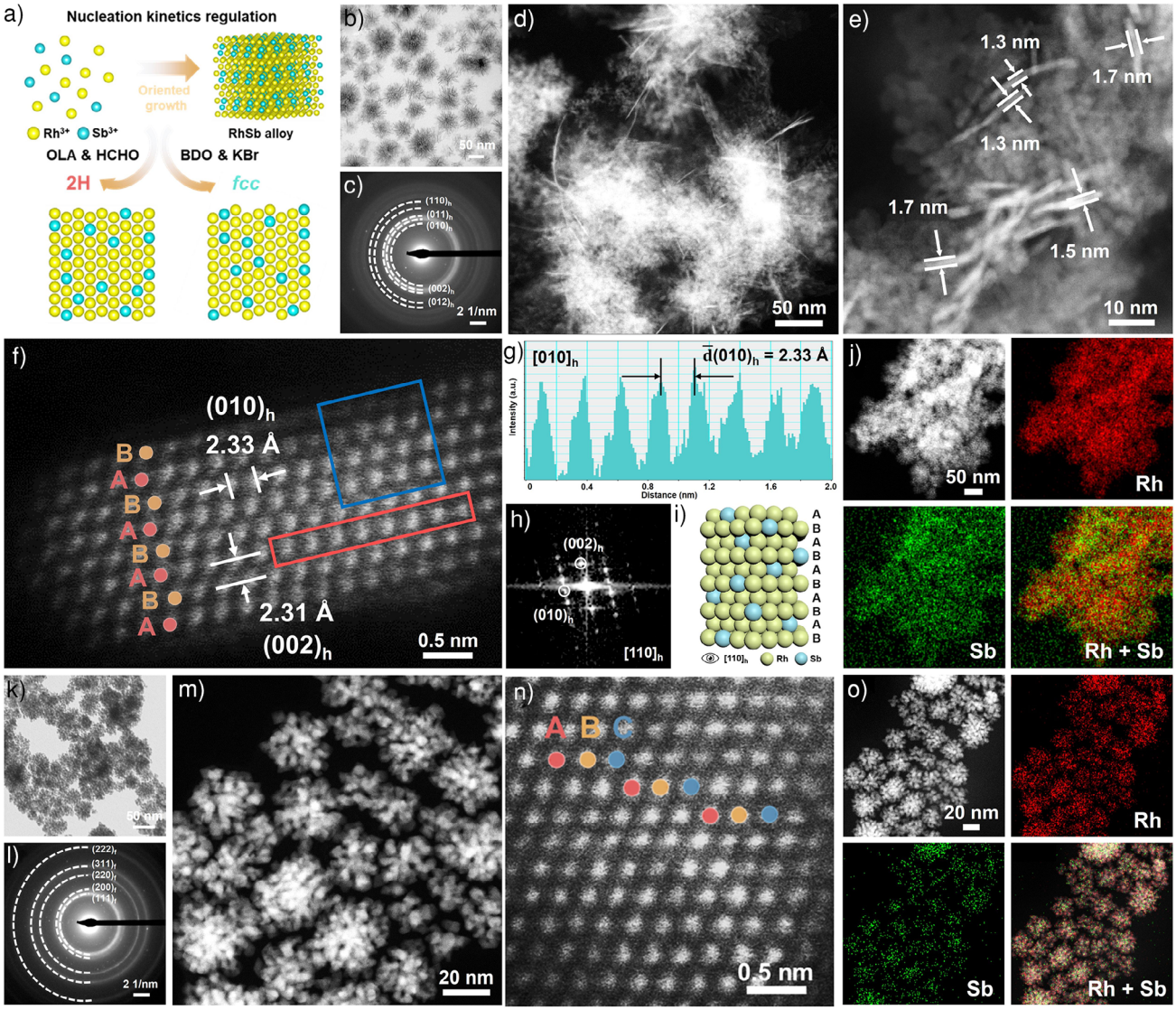

Figure 1. Synthesis and structural characterizations. a) Schematic illustration for the synthetic process of unconventional 2H-phase and fcc-phase RhSb alloys. OLA, oleic acid; BDO, 1,2-butanediol. b) and c) TEM image (b) and corresponding SAED pattern (c) of 2H RhSb NFs. d) and e) Low-magnification (d) and high-magnification (e) HAADF-STEM images of 2H RhSb NFs. f) Atomic-resolution HAADF-STEM image of 2H RhSb NFs. g) Integrated pixel intensity profile derived from the area marked by red rectangle in (f). h) Corresponding FFT pattern taken from the region marked by blue square in (f). i) Atomic model of 2H RhSb NFs. j) HAADF-STEM image and the corresponding EDS elemental maps of 2H RhSb NFs. k) and l) TEM image (k) and corresponding SAED pattern (l) of fcc RhSb NDs. m) and n) High-magnification (m) and atomic-resolution (n) HAADF-STEM images of fcc RhSb NDs. o) HAADF-STEM image and the corresponding EDS elemental maps of fcc RhSb NDs.

generating varied phase structures. Transmission electron microscopy (TEM) images (Figures 1b and S1) show that the as-prepared 2H RhSb NFs present a nanometer-sized self-assembly morphology in which 2D ultrathin nanosheets are interconnected. Notably, the corresponding selected area electron diffraction (SAED) pattern (Figure 1c) verifies the 2H phase of RhSb NFs as the characteristic diffraction rings can be clearly observed. The detailed microstructures are explored by aberration-corrected high-angle annular dark-field scanning TEM (HAADF-STEM). As shown in Figures 1d,e and S2, the assembled nanosheets in 2H RhSb NFs exhibit a few-layer nature with a thickness of about 1.5 nm (~6 to 7 atomic layers). Moreover, some pits and holes are observed on the basal plane of nanosheets, which could generate abundant low-coordinated active sites. More importantly, in the atomic-resolution HAADF-STEM image of a typical nanosheet viewed from the $[110]_h$ zone axis (Figure 1f), the atomic arrangement shows a characteristic "AB" stacking sequence assigned to the 2H phase. In addition, the interplanar spacings assigned to the $(010)_h$ and $(002)_h$ facets are measured as 2.33 and 2.31 Å, respectively, with the integrated intensity profile of atoms on the $(010)_h$ plane marked with a red rectangle shown in Figure 1g. The corresponding fast Fourier transform (FFT) pattern (Figure 1h) of the selected area marked with a blue square in Figure 1f is also in accordance with 2H phase, based on

which an atomic model of 2H RhSb NFs is schematically presented in Figure 1i. Moreover, the X-ray diffraction (XRD) pattern further verifies the 2H phase of as-prepared RhSb NFs (Figure S3). Scanning electron microscopy-energy dispersive X-ray spectroscopy (SEM-EDS) (Figure S4) shows that the atomic ratio of Sb in 2H RhSb NFs is around 15%. HAADF-STEM image and the corresponding EDS elemental maps (Figure 1j) indicate the alloy structure of 2H RhSb NFs with a homogeneous distribution of both Rh and Sb elements.

Without the addition of Sb, the as-synthesized Rh NFs exhibit a higher self-assembly degree compared to 2H RhSb NFs, while they maintain the 2H phase according to the analysis of SAED and XRD patterns (Figures S5 and S6). In contrast, TEM images (Figures 1k and S7) of as-synthesized fcc RhSb NDs show a uniform dendrite-like morphology. The diffraction rings in the corresponding SAED pattern (Figure 1l) are attributed to the fcc phase. From the HRTEM (Figure S8) and HAADF-STEM images (Figure 1m), it can be seen that each dendrite-like nanoassembly is constituted by small nanoplates with an overall lateral size of 20–50 nm. Notably, a characteristic "ABC" stacking sequence of fcc phase along the $[111]_f$ close-packed direction can be clearly identified from the HAADF-STEM image (Figure 1n). XRD pattern (Figure S9) indicates that the structure of RhSb NDs is well consistent with that of the standard *fcc*-phase Rh except for slight peak shifts, further their fcc phase (Figure S10). EDS spectrum (Figure S11) shows that the atomic ratio of Rh/Sb is around 85/15, similar to that of 2H RhSb NFs. Moreover, the HAADF-STEM image and corresponding elemental maps of fcc RhSb NDs (Figure 1o) demonstrate the uniform distribution of Sb in Rh matrix.

X-Ray Spectral Analysis

The chemical state and coordination environment evolutions after alloying and phase regulation were further investigated by X-ray spectroscopies. From the high-resolution X-ray photoelectron spectroscopy (XPS) spectra of Rh 3*d* (Figure 2a), it can be seen that the Rh metallic state dominates in all prepared samples but with the existence of Rh^{3+} owing to the inevitable oxidation in air. For 2H Rh NFs, two peaks attributed to the $3d_{3/2}$ and $3d_{5/2}$ doublet of Rh^0 are located at 311.5 and 307.0 eV, respectively. Interestingly, these two peaks in 2H RhSb NFs and fcc RhSb NDs both shift toward the higher binding energy positions, indicating the change of electronic state in Rh after alloying with Sb (Figure S12). Besides, ultraviolet photoelectron spectroscopy (UPS) was used to further verify the electronic state disparity (Figure 2b). Based on the measured photoemission cut-off voltages ($E_{cut\text{-}off}$), the work function (W_f) of 2H RhSb NFs, fcc RhSb NDs, and 2H Rh NFs are calculated as −4.31, −4.17, and −3.86 eV, respectively (Figure 2c). This indicates that the alloying effect will induce the electron transfer from Rh to Sb, thus promoting the upper shift of the relative Fermi level (E_F). More importantly, the W_f of 2H RhSb NFs is higher than that of fcc RhSb NDs, which suggests that phase engineering can further tune the electronic distribution of RhSb alloy.

More details on the electronic structures and coordination environments of the as-synthesized samples were explored by X-ray absorption spectroscopy (XAS). As shown in Figure 2d, the X-ray absorption near-edge structure (XANES) spectra of 2H Rh NFs present a white line position where its located energy region almost coincides with the Rh foil. By contrast, the white line positions of 2H RhSb NFs and fcc RhSb NDs are situated in the middle of Rh foil and Rh_2O_3, indicating that Rh atoms in RhSb nanoalloys function as an electron donor and this electron-donating effect is further prominent in the 2H-phase matrix. Figure 2e shows the k^2-weighted Fourier-transform Rh K-edge extended X-ray absorption fine structure (EXAFS) spectra. Compared with the dominant peaks at 2.41 Å attributed to the Rh-Rh scattering path of 2H Rh NFs and Rh foil in R space, both 2H RhSb NFs and fcc RhSb NDs exhibit their dominant peaks at 2.55 Å, corresponding to the Rh-Rh/Rh-Sb scattering paths. This change of metal-metal bond length can be attributed to the formation of RhSb alloy nanostructures. The coexistence of Rh–O scattering paths in samples may be ascribed to the oxidation in air. The fitting results of R space (Figure 2f and Table S1) show that the Rh—Sb bond lengths in 2H RhSb NFs and fcc RhSb NDs are both longer than the Rh—Rh bond length. The coordination numbers (CNs) of Rh atoms in 2H RhSb NFs (8.1) and fcc RhSb NDs (8.3) are similar and slightly lower than those in 2H Rh NFs (9.1). The fitting results of k space are presented in Figure S13. Moreover, the wavelet transforms (WTs) of Rh K-edge EXAFS spectra show that 2H RhSb NFs and fcc RhSb NDs share similar coordination patterns (Figure 2g), which are significantly different from 2H Rh NFs. Differently, the center of maximum intensity after alloying exhibits an increase in R-range but an obvious decrease in k-range due to the variation of coordination environment.

Electrochemical NO_2RR Performance

The as-synthesized RhSb alloy nanostructures were used as the catalysts for electrochemical NO_2RR. Typically, the electrocatalytic performance was tested in a H-type cell with the electrolyte containing 0.5 M K_2SO_4 and 100 mM KNO_2. As shown in Figure 3a, the linear scan voltammetry (LSV) curves of 2H RhSb NFs and fcc RhSb NDs exhibit much higher current densities than 2H Rh NFs with the addition of NO_2^-, demonstrating higher electrocatalytic activities for NO_2RR. The peak currents of these three samples appearing from −0.2 to −0.4 V (vs. RHE) are ascribed to the limited mass transfer, in which NO_2RR plays a more dominant role than hydrogen evolution reaction (HER). The calculated Tafel slope of 2H RhSb NFs is 94 mV dec^{-1}, much lower than that of fcc RhSb NDs (140 mV dec^{-1}) and 2H Rh NFs (166 mV dec^{-1}), owing to the smaller polarization of 2H RhSb NFs during NO_2RR (Figure S14). The NO_2RR performance was further evaluated by chronoamperometry (CA) measurement for 1 h in the potential range from −0.1 to −0.6 V (vs. RHE), after which the product was detected by ultraviolet–visible (UV–vis) method and quantified by comparing with the calibration curve of NH_4^+ concentration (Figures S15 and S16). As a

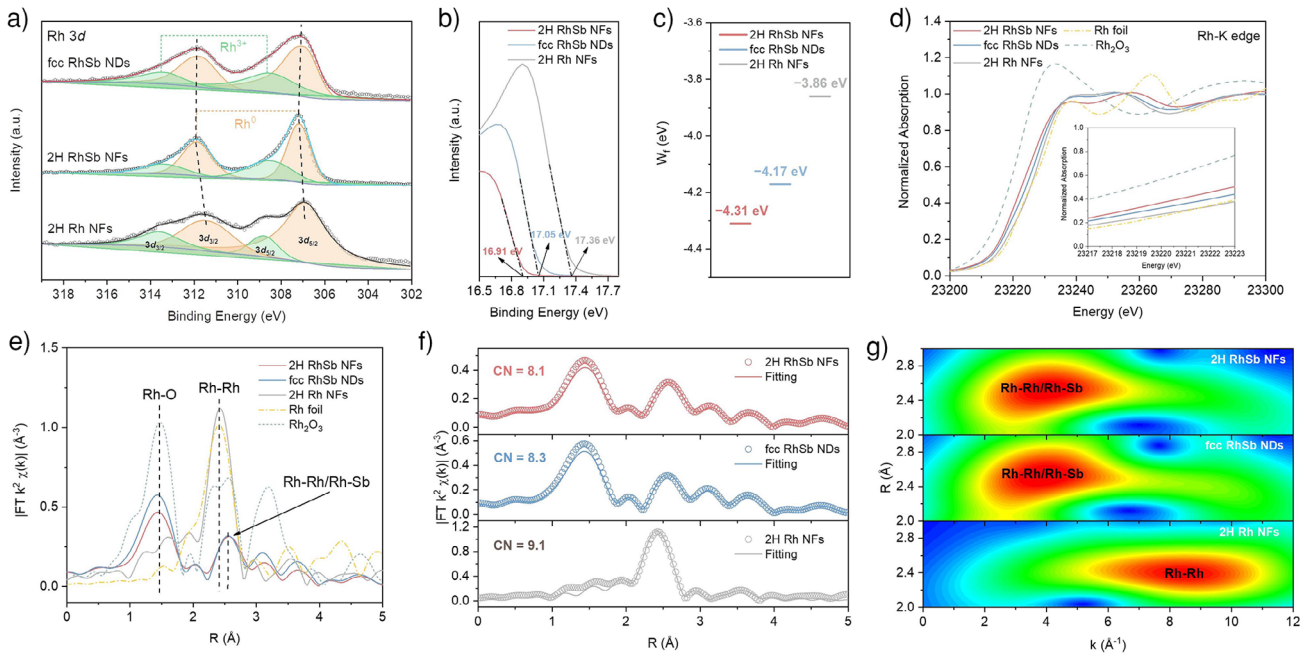

Figure 2. X-ray spectral analysis. a) High-resolution XPS spectra of Rh 3*d* for 2H RhSb NFs, fcc RhSb NDs, and 2H Rh NFs. b) and c) Photoemission cut-off spectra (b) and the calculated W_f (c) of 2H RhSb NFs, fcc RhSb NDs, and 2H Rh NFs. d) Normalized Rh K-edge XANES spectra with the reference samples of Rh foil and Rh_2O_3 for comparison. Inset: The detailed white line positions. e) Fourier transform of k^2-weighted EXAFS spectra. f) and g) R-space EXAFS fitting (f) and wavelet transform (g) of 2H RhSb NFs, fcc RhSb NDs, and 2H Rh NFs.

consequence, 2H RhSb NFs deliver the highest FE of 96.8% at −0.3 V (vs. RHE), while the FEs of fcc RhSb NDs and 2H Rh NFs are determined as 92.9% and 82.4%, respectively (Figure 3b). It's worth noting that 2H RhSb NFs demonstrate the highest FE value among three samples at each applied potential. Correspondingly, the NH_3 partial current densities (j_{NH3}) of 2H RhSb NFs are also remarkably larger than those of the other two catalysts (Figure 3c), in which the largest j_{NH3} can reach up to 89.3 mA mg_{cat}^{-1}. Higher j_{NH3} indicates that more electrons participate in the NO_2RR process for efficient NH_3 production. Expectedly, 2H RhSb NFs exhibit the highest NH_3 yield rate of 47.2 mg h^{-1} mg_{cat}^{-1} at −0.6 V (vs. RHE), which is almost 1.34 and 1.69 times that of fcc RhSb NDs and 2H Rh NFs, respectively (Figure 3d). Such results elucidate that the alloying and phase engineering for RhSb nanostructures can synergistically improve the electrocatalytic activity of NO_2RR. To visually display the superior NO_2RR performance of 2H RhSb NFs for efficient NH_3 production, a comparison of performance parameters with the other previously reported catalysts for NO_2RR in neutral conditions is shown in Table S2.[13,25,56–63]

The ^1H nuclear magnetic resonance (NMR) spectroscopy was utilized to quantify the generated NH_3. As shown in Figure 3e, three characteristic peaks assigned to NH_4^+ species are clearly observed with the presence of 100 mM KNO_2 in electrolyte at an applied potential of −0.3 V (vs. RHE), while no obvious peak can be found in the absence of KNO_2. The calculated NH_3 FE and yield rate by ^1H NMR method are well consistent with those determined by UV–vis method (Figures 3f and S17). Moreover, the NO_2RR performance in the low-concentration NO_2^- was explored using 2H RhSb NFs as the electrocatalyst (Figures S18 and S19). It can be seen that even when the NO_2^- concentration decreases to 10 mM, the highest NH_3 FE can still maintain above 80% at −0.3 V (vs. RHE) and the largest NH_3 yield rate can achieve 18.8 mg h^{-1} mg_{cat}^{-1} at −0.6 V (vs. RHE) (Figures 3g and S20), demonstrating impressive potential for effluent treatment toward NH_3 production. The catalytic durability of 2H RhSb NFs was further evaluated by the consecutive CA test (Figure S21). During the 30 continuous electrolysis cycles at −0.3 V (vs. RHE), the NH_3 FE remains stable (~95%) and the corresponding yield rate keeps a steady level without large attenuation (Figure 3h). Importantly, the morphology, structure, and composition of 2H RhSb NFs are well preserved after the long-term electrolysis (Figures S22 and S23).

Mechanism Investigation

To deeply explore the synergistic effects of alloying and phase engineering on the improved NO_2RR performance of 2H RhSb NFs, the ex/in situ characterizations were conducted. As shown in Figure 4a, the desorption peak of H* can be clearly observed at the potential from −0.2 to 0 V (vs. RHE) in the CV curves tested in 1.0 M KOH solution. As a result, the capacity of H* desorption on 2H RhSb NFs is much higher than those on fcc RhSb NDs and 2H Rh NFs based on the evaluation of H* desorption current density. This indirectly suggests that 2H RhSb NFs enable the supply of abundant H* during NO_2RR for favorable hydrogenation process. Furthermore, *tert*-butyl

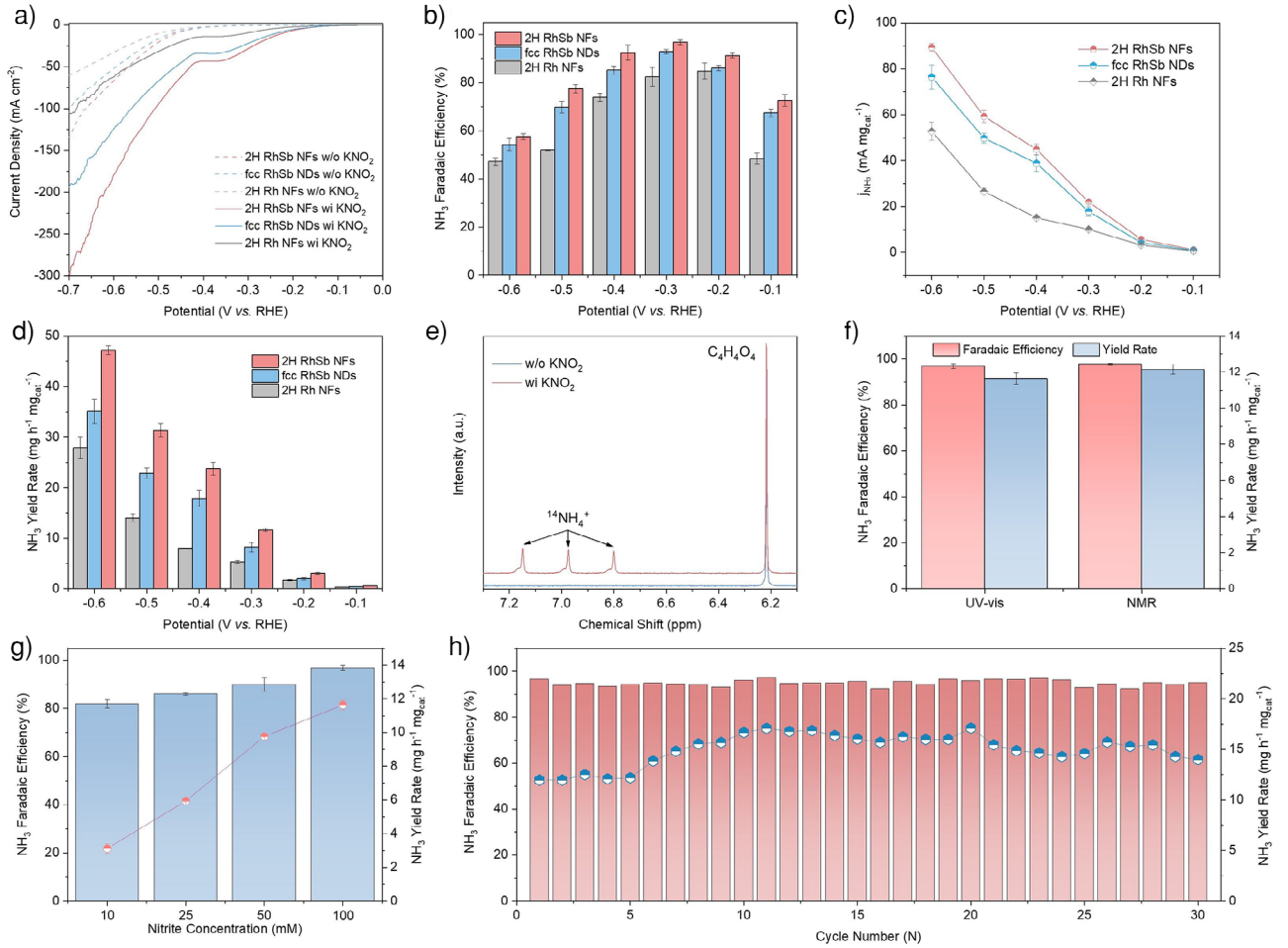

Figure 3. Electrocatalytic NO_2RR performance. a) LSV curves of 2H RhSb NFs, fcc RhSb NDs, and 2H Rh NFs in neutral 0.5 M K_2SO_4 solution in the presence (solid lines) and absence (dashed lines) of 100 mM KNO_2. b)–d) NH_3 FE (b), partial current density (c), and yield rate (d) of 2H RhSb NFs, fcc RhSb NDs, and 2H Rh NFs under different applied potentials. e) The ^1H NMR spectra of electrolytes for 2H RhSb NFs after 1-h electrolysis at −0.3 V (vs. RHE). f) NH_3 FE and yield rate comparison of 2H RhSb NFs at −0.3 V (vs. RHE) by both UV–vis and ^1H NMR methods. g) NH_3 FE and yield rate of 2H RhSb NFs at −0.3 V (vs. RHE) in electrolytes with different concentrations of NO_2^-. h) NH_3 FE and yield rate of 2H RhSb NFs with 1-h electrolysis at −0.3 V (vs. RHE) for 30 cycles.

alcohol (TBA) was introduced into the electrolyte to trap H* on 2H RhSb NF electrode (Figure 4b). With the increase of TBA concentration, the NH_3 yield rate shows a dramatic decrease, indicating the critical role of H* formation in NH_3 production. Meanwhile, the electrochemically active surface area (ECSA) was measured by the electrochemical double-layer capacitance (C_{dl}) (Figure S24). The C_{dl} of 2H RhSb NFs could deliver up to 2.84 mF cm^{-2}, higher than those of fcc RhSb NDs (2.48 mF cm^{-2}) and 2H Rh NFs (1.86 mF cm^{-2}) (Figure 4c), indicating more electrocatalytically active sites on 2H RhSb NFs. The kinetic isotope effect (KIE) using D_2O solvent to replace H_2O in the electrolyte was also carried out (Figure 4d), which was typically defined as the ratio of NH_3 yield rate in H_2O to D_2O. The magnitude of KIE value can display the proton's effect on the rate-determining step (RDS) in H_2O-involved reactions and evaluate the water activation property of catalyst. As shown in Figure 4e, 2H Rh NFs exhibit the highest KIE value of 1.77 due to the sluggish H_2O dissociation for H* generation, while the KIE values of fcc RhSb NDs and 2H RhSb NFs are determined as 1.40 and 1.19, respectively, indicating the kinetically accelerated H_2O dissociation after alloying and phase engineering.

In situ differential electrochemical mass spectrometry (DEMS) was further utilized to obtain a comprehensive insight into the reaction pathway of NO_2RR. With five cycles of the LSV scanning, the mass/charge (m/z) signals of 2, 14, 15, 16, 17, 28, 30, 31, 33, 44, and 46 assigned to H_2, N, NH, NH_2, NH_3, N_2, NO, HNO/NOH, NH_2OH, N_2O, and NO_2, respectively, were all detected for 2H RhSb NFs and fcc RhSb NDs. Generally, there are mainly three reaction pathways according to previous reports (Figure S25): i) $NO_2^* \rightarrow NO^* \rightarrow N^* \rightarrow NH^* \rightarrow NH_2^* \rightarrow NH_3^*$; ii) $NO_2^* \rightarrow NO^* \rightarrow NOH^* \rightarrow N^*$ (HNOH*) $\rightarrow NH^* \rightarrow NH_2^* \rightarrow NH_3^*$; iii) $NO_2^* \rightarrow NO^* \rightarrow HNO^* \rightarrow HNOH^* \rightarrow H_2NOH^* \rightarrow NH_2^* \rightarrow NH_3^*$. As shown in Figure 4f,g, the signals of N* and HNO*/NOH* are very strong in sharp contrast to the weak intensities of NH_2OH^* for both 2H RhSb NFs and fcc RhSb NDs, suggesting that the NO_2RR reaction pathways of these two samples might be dominated by the aforementioned i) and/or ii). More importantly, the signal magnitudes of

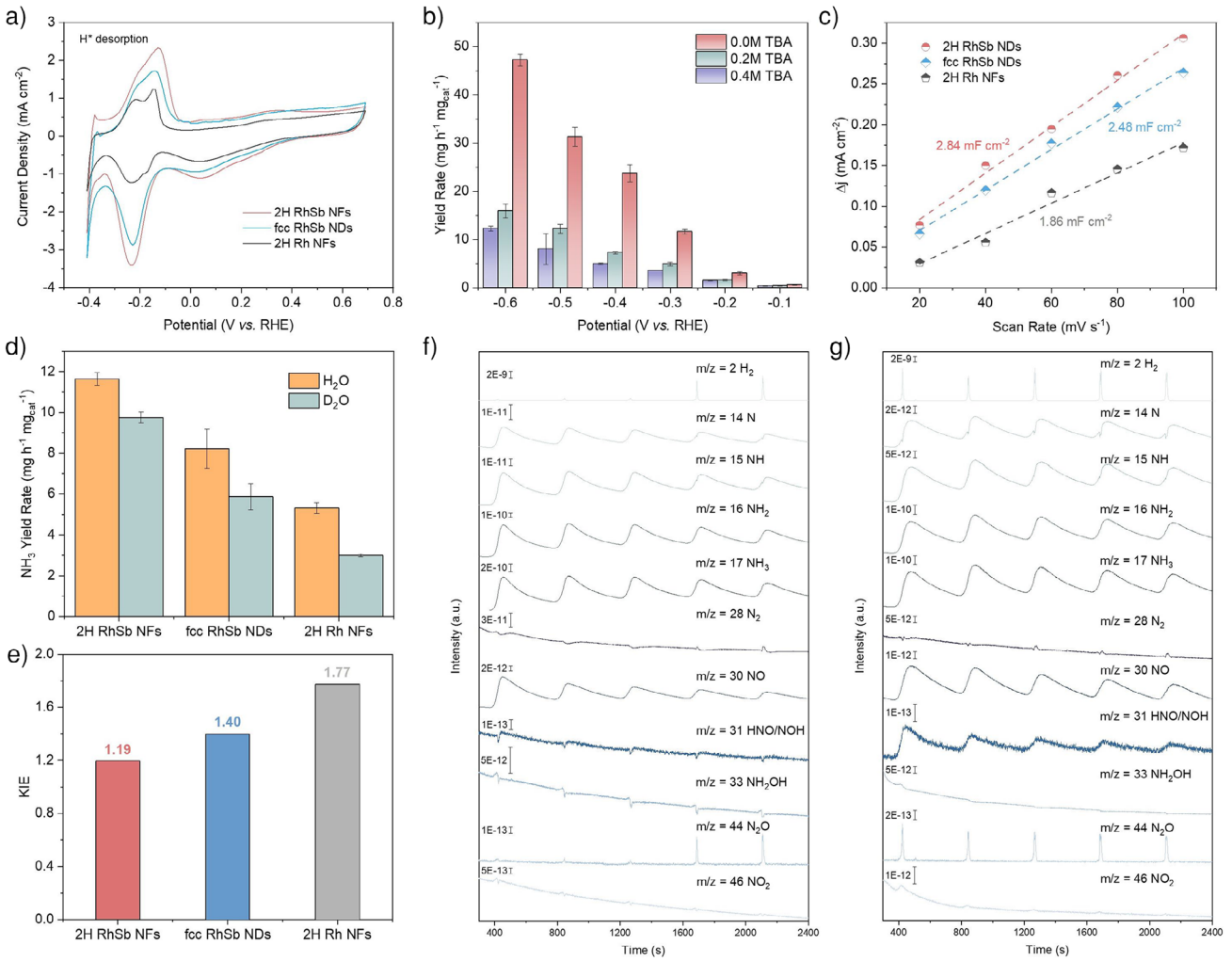

Figure 4. Ex/in situ electrochemical mechanism investigation. a) CV curves of 2H RhSb NFs, fcc RhSb NDs, and 2H Rh NFs in 1.0 M KOH solution. b) NH_3 yield rate of 2H RhSb NFs in the electrolytes with different TBA concentrations at various potentials. c) Fitting results of C_{dl} for 2H RhSb NFs, fcc RhSb NDs, and 2H Rh NFs. d) and e) NH_3 yield rate (d) and KIE diagram (e) for the ratio of NH_3 yield rate in H_2O to D_2O solvents in 0.5 M K_2SO_4 solution with 100 mM NO_2^- at −0.3 V (vs. RHE). f) and g) In situ DEMS patterns of 2H RhSb NFs (f) and fcc RhSb NDs (g).

some critical nitrogen-containing intermediates (including N*, NH*, NH_2*, and HNO*/NOH*) detected on 2H RhSb NFs are all higher than those on fcc-phase counterpart (Figure S26), demonstrating more favorable hydrogenation kinetics of the former for NH_3 production. Expectedly, the NH_3 signal intensity of 2H RhSb NFs is much higher (Figure S27), which may also explain the reason why 2H RhSb NFs deliver the higher NH_3 FE and yield rate. Moreover, the more positive onset potential for H_2 formation and weaker H_2-signal peak intensity of 2H RhSb NFs compared to fcc RhSb NDs suggest that the energy barrier of the generated H* for NO_2RR is lower on 2H RhSb NFs, which also enable the HER process more inhibited.

Theoretical Calculations

To understand the origins of excellent NO_2RR performances of 2H RhSb NFs, DFT calculations were carried out to compare the distinct electronic structures and reaction trends of 2H and fcc RhSb nanostructures. The electronic distributions regarding the bonding and antibonding orbitals near the E_F show stronger distributions on the surface of 2H phase, indicating more electroactive electrons on 2H RhSb surfaces to facilitate the electrocatalysis (Figure 5a,b). The Sb sites on 2H RhSb display much stronger bonding orbital distributions to facilitate surface electron transfer and exchange. For both 2H and fcc surfaces, it was noticed that the surface Sb sites experience slight distortions with prolonged Rh─Sb bond lengths than Rh─Rh bonds, which is supportive of experimental characterizations. Then, the projected partial density of states (PDOS) is supplied to further compare the overall electronic structures for RhSb alloys with different phases (Figure 5c,d). Notably, the overall PDOS of 2H and fcc phases are relatively similar, where Rh–4*d* orbitals dominate near the E_F as the main active sites. The Sb–5*p* orbitals are broadly distributed and cross the E_F, which pins the Rh–4*d* orbitals to play as protection

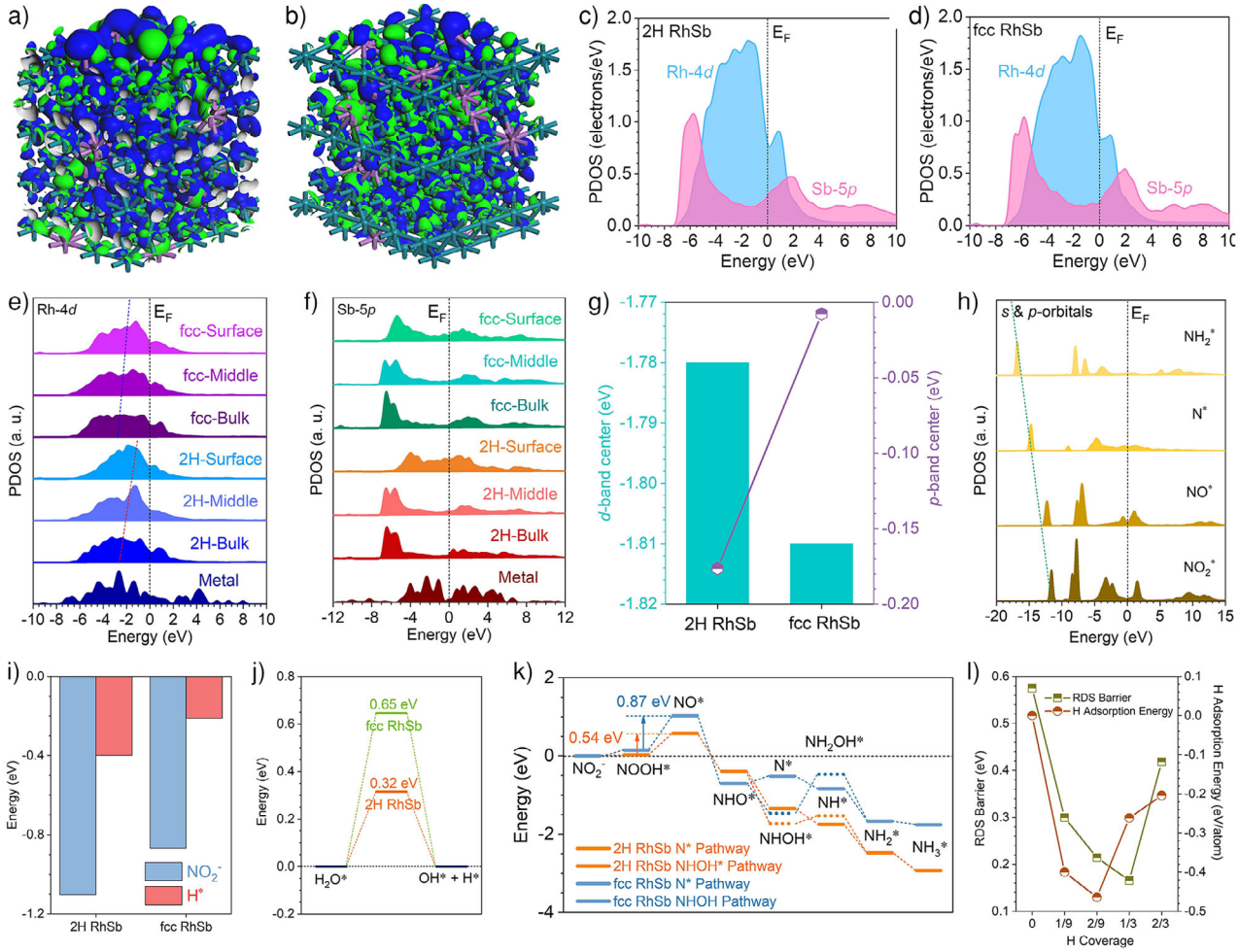

Figure 5. Theoretical calculations of NO_2RR on RhSb alloy nanostructures with different phases. a) and b) The electronic distributions of bonding and antibonding orbitals near E_F on a) 2H RhSb and b) fcc RhSb. Cyan balls = Rh and purple balls = Sb. Blue isosurface = bonding orbitals and green isosurface = antibonding orbitals. c) and d) PDOS of (c) 2H RhSb and (d) fcc RhSb. e) and f) PDOS comparisons of (e) Rh-4*d* and f) Sb-5*p*. g) The *d*- and *p*-band center comparisons. h) The PDOS of key NO_2RR intermediates adsorbed on the 2H RhSb. i) The adsorption energy of NO_2^- and protons on 2H RhSb and fcc RhSb. j) The water dissociation energy of 2H RhSb and fcc RhSb. k) The reaction trends of NO_2RR on 2H RhSb and fcc RhSb. l) The evolution of RDS barriers and adsorption energies for different H coverages.

sites to stabilize the electronic structures of active sites. As for the surface electronic structure, the overlapping between the Rh–4*d* and Sb–5*p* orbitals is stronger in the 2H phase than in the *fcc* phase (Figure S28), which indicates the enhanced *p*–*d* orbital coupling to regulate the electroactivity of the surface. Specifically, the stronger interactions with neighboring Rh sites on the 2H-phase surface can modulate the Sb–5*p* orbitals to become more concentrated near the E_F. Accordingly, a schematic diagram is provided in Figure S29 to illustrate the enhanced *p*–*d* orbital coupling effect. For the conventional *fcc* phase, there is relatively small overlapping between the Rh–4*d* and Sb–5*p* orbitals, which can only regulate the electroactivity of the Rh sites at a very limited level. With the phase transition from *fcc* to 2H, the Rh–4*d* orbitals not only upshift toward the E_F but also become more concentrated. Meanwhile, the Sb–5*p* orbitals turn highly concentrated near the E_F, supplying the strong *p*–*d* orbital coupling with Rh–4*d* orbitals to promote the electron transfer efficiency of Rh sites for NO_2RR. Through the *p*–*d* orbital couplings, the valence states of Rh will be maintained to guarantee highly robust electroactivity for NO_2RR. In order to reveal the superior performance of the 2H phase over the *fcc* phase for RhSb, the site-dependent PDOS has been demonstrated to show the detailed electronic structure evolutions (Figure 5e). Compared to the pristine bulk metals of Rh and Sb, the evident PDOS changes of RhSb support the strong interactions induced between Rh and Sb in the alloys. For Rh sites in the 2H RhSb, the electronic modulations from bulk to the surface are obvious, where the 4*d* orbitals are evidently more concentrated with formed peaks close to the E_F. In contrast, the Rh–4*d* orbitals in fcc RhSb are less sensitive with a weaker upshifting trend to the E_F, supporting the higher electroactivity of active sites in 2H RhSb. For the Sb–5*p* orbitals in 2H RhSb, the surface sites exhibit different electronic structures, where 5*p* orbitals become highly concentrated with the significantly increased electron density near the E_F, supplying efficient electron transfer trends (Figure 5f). Although the gradual upshifting

trend of Sb–5*p* orbitals is also noted in the *fcc* phase, the corresponding changes of PDOS are weaker than that of 2H RhSb. Accordingly, the surface Sb sites in 2H RhSb are more active to promote surface electron transportations to achieve efficient NO_2RR. To understand the interactions between Rh and Sb sites, the *d*-band center and *p*-band centers are compared (Figure 5g). The 2H RhSb possesses a higher *d*-band center and lower *p*-band center than the fcc RhSb, which is attributed to the stronger interactions between Rh and Sb. This results in more electron transfer from Rh to Sb as well as the decrease of W_f, enhancing the electroactivity of active sites. Besides the electronic structures of RhSb, the PDOS evolutions of key adsorbates during NO_2RR are also important (Figure 5h). From NO_2* to NH_2*, the downshifting trends of *s*- and *p*-orbitals display a good linear relationship except for the deviation of NO*, revealing that the conversion from NO_2^- to NO* is the potential RDS.

From the energetic perspective, the adsorption preferences of key reactants upon NO_2RR were first compared (Figure 5i). 2H RhSb shows the lower adsorption energies of NO_2^-, promoting the activation toward NO_2RR. The stronger adsorption of protons in the 2H phase also suppresses the competitive HER process. Meanwhile, the water dissociation determines the generation of active protons, where 2H RhSb requires a 0.32 eV barrier (Figure 5j). Compared to the fcc RhSb, the much smaller barrier scales guarantee the efficient supply of active protons during the NO_2RR on the 2H RhSb. For the whole reaction trends, the conversion of NOOH* to NO* shows the largest energy barrier as the RDS, which is 0.54 and 0.87 eV for the 2H RhSb and fcc RhSb, respectively (Figure 5k). For the competitive N* and NHOH* pathways, the initial formation of NHOH* is slightly more energetically favored. However, the following formation of NH_2OH* meets an energy barrier of 0.20 and 0.99 eV for 2H RhSb and fcc RhSb, respectively, demonstrating that the NHOH* pathway is less preferred than the N* pathway for NO_2RR. Due to the much reduced energy barrier of RDS and stronger overall reaction trend, the 2H RhSb displays superior NO_2RR performances. In addition, the influences of the proton coverage for the RDS barrier were also explored on the 2H RhSb (Figure 5l). As the proton coverage increases, both the adsorption energy costs of protons and the RDS barriers will decrease firstly and then increase, which indicates that high proton coverage is not beneficial for the NO_2RR. Based on the results, the RDS reduces to the lowest point at a proton coverage of 2/9. The further increases in the proton coverage potentially block the active sites and increase the RDS barriers. Therefore, the strong adsorption of reactants, fast water dissociation, and lower reaction barriers lead to the excellent NO_2RR performances of 2H RhSb.

Demonstration of Rechargeable Zinc-Nitrite/Methanol Batteries

NH_3 with a high energy density of 4.32 kWh L^{-1} can function as a potential medium in both chemical engineering and energy storage. In light of this, the zinc-nitrate/nitrite (Zn-NO_x^-) batteries are explored to integrate NH_3 production and sewage disposal by the energy device, in which a high energy density can be accessible via nitrate reduction reaction (NO_3RR) or NO_2RR. However, the rechargeability of traditional Zn-NO_x^- batteries is poor since a large energy barrier needs to be overcome for OER during charging on normally designed catalysts. Considering this crucial issue, methanol oxidation reaction (MOR) was applied to the as-synthesized RhSb nanostructures to replace the kinetically sluggish OER upon charging. By coupling with the NO_2RR to construct the Zn-NO_2^-/MeOH batteries (Figure S30), the rechargeability would be significantly improved due to the efficient energy transfer. As shown in Figure S31, the open-circuit voltage (OCV) of Zn-NO_2^-/MeOH batteries with 2H RhSb NFs and fcc RhSb NDs cathodes both can be maintained at ~1.50 V (vs. Zn^{2+}/Zn). Thanks to the excellent NO_2RR activity, the maximum power density of Zn-NO_2^-/MeOH batteries with 2H RhSb NFs reached up to 4.63 mW cm^{-2}, higher than that (3.70 mW cm^{-2}) of fcc RhSb NDs (Figure 6a). Figure 6b shows the rate capability of 2H RhSb NFs and fcc RhSb NDs cathodes upon discharging. The discharge plateaus of 2H RhSb NFs were around 1.47, 1.44, 1.32, 0.85, 0.77, 0.63, and 0.46 V (vs. Zn^{2+}/Zn) at 0.1, 0.2, 0.5, 1.0, 2.0, 5.0, and 10.0 mA cm^{-2}, respectively, which were all higher than those of fcc RhSb NDs. With the backed operation at low rates (0.1 and 0.5 mA cm^{-2}), the working voltages of batteries still maintained close to the initial states. And the NH_3 FE of 2H RhSb cathode could achieve above 90% at all tested current densities with the highest yield rate of 4.83 mg h^{-1} mg_{cat}^{-1} at 10.0 mA cm^{-2} (Figure S32). More surprisingly, the assembled Zn-NO_2^-/MeOH batteries with 2H RhSb NFs could deliver the electric energy of 89.1 and 58.9 mWh when fully discharged to 0.005 V (vs. Zn^{2+}/Zn) at 0.5 and 1.0 mA cm^{-2}, respectively (Figure 6c). To demonstrate the rechargeability, the round-trip discharging/charging tests at various rates were carried out (Figures 6d and S33). It can be seen that the voltage polarizations of batteries with 2H RhSb cathodes are alleviated with the addition of MeOH in the electrolyte. The well voltage recovery of batteries at 0.1 mA cm^{-2} indicates the good structural reliability of 2H RhSb NFs as a bifunctional catalyst. Impressively, the highest round-trip energy efficiency of as-constructed Zn-NO_2^-/MeOH batteries with 2H RhSb cathodes could reach up to 96.4% at 0.1 mA cm^{-2}, higher than that (93.0%) of the corresponding Zn-NO_2^- counterparts (Figure 6e). This disparity was further magnified at higher current densities, and the Zn-NO_2^-/MeOH batteries using 2H RhSb cathodes also showed performance superiority compared to batteries using fcc RhSb cathodes (Figure S34). LSV tests were carried out to verify the crucial role of MOR in the improved battery performance (inset in Figure 6e). With a typical current density limit of 1.0 mA cm^{-2}, the voltage gap between MOR and OER processes on 2H RhSb electrodes achieved 342 mV, meaning that the energy consumption will be decreased with MOR during charging. Furthermore, the long-term cycling tests were performed for these two battery prototypes. At 1.0 mA cm^{-2}, the Zn-NO_2^-/MeOH batteries exhibited a smaller discharge/charge voltage gap and maintained stable working for 120 h (60 cycles) (Figure 6f), presenting impressive rechargeability and durability. In this process, the corresponding discharge/charge end potentials

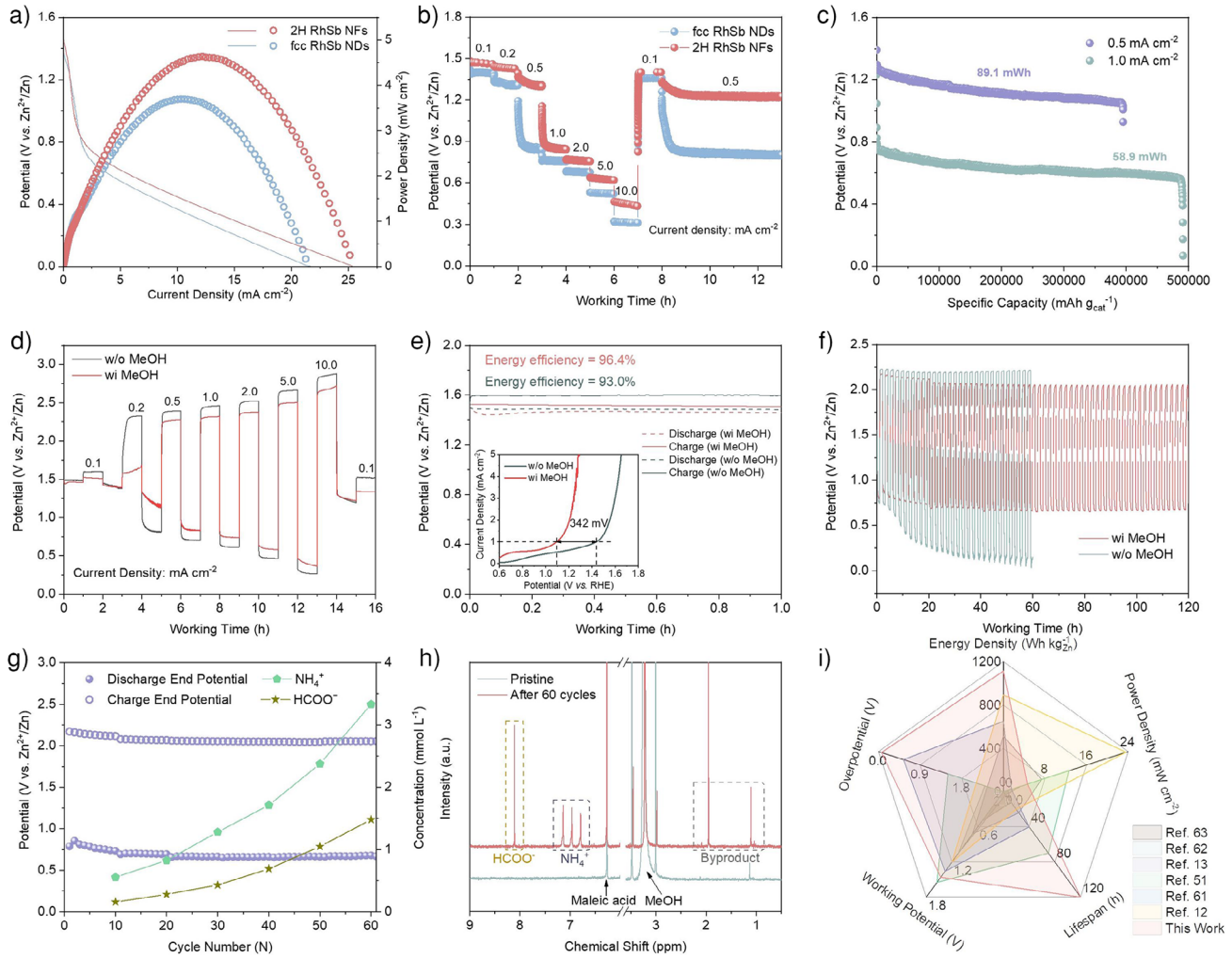

Figure 6. Electrochemical performances of rechargeable Zn-NO_2^-/MeOH batteries. a) Discharging polarization profiles and resultant power density curves of Zn-NO_2^-/MeOH batteries. b) Rate capabilities of Zn-NO_2^-/MeOH batteries upon discharging. c) Galvanostatic discharge profiles of Zn-NO_2^-/MeOH batteries with 2H RhSb NF cathodes from OCV to 0.005 V (vs. Zn^{2+}/Zn) at 0.5 and 1.0 mA cm^{-2}. d) and e) Round-trip discharge/charge profiles of as-assembled Zn-NO_2^-/MeOH and Zn-NO_2^- batteries with 2H RhSb NF cathodes at various current densities (d) and 0.1 mA cm^{-2} (e), respectively. Inset in (e): LSV curves from 0.6 to 1.8 V (vs. RHE) of 2H RhSb NFs in the electrolytes with (red line) and without (cyan line) MeOH. f) Long-term cycling stability test of Zn-NO_2^-/MeOH and Zn-NO_2^- batteries at 1.0 mA cm^{-2}. g) Discharge/charge end potentials of Zn-NO_2^-/MeOH batteries and the calculated concentration evolutions of both NH_4^+ and $HCOO^-$ upon cycling. h) ^{1}H NMR spectra of the pristine cathodic electrolyte and that taken from the Zn-NO_2^-/MeOH batteries after the 60th cycle. i) The comprehensive comparison of as-assembled Zn-NO_2^-/MeOH batteries using 2H RhSb NF cathodes with the battery performances of other reported catalysts.

of Zn-NO_2^-/MeOH batteries were recorded, and the concentration evolutions of both NH_3 (discharge product) and HCOOH (charge product) were also investigated (Figures 6g and S35). Notably, the concentration of generated HCOOH at the 60th cycle reached 1.48 mmol L^{-1}. The ^{1}H NMR spectra indicated the formation of both NH_3 and HCOOH in the cathodic electrolyte of Zn-NO_2^-/MeOH batteries after cycling (Figure 6h). The morphology, structure, and composition of 2H RhSb NFs were well preserved with such long-term round-trip operation (Figures S36 and S37). Compared with the other reported Zn-NO_3^- and Zn-NO_2^- batteries, the as-designed rechargeable Zn-NO_2^-/MeOH batteries present impressively comprehensive performance (Figure 6i and Table S3).[12,13,54,64–66] Generally, regardless of some parasitic reactions (e.g., HER and OER), the theoretical working mechanisms of as-assembled Zn-NO_2^-/MeOH batteries can be described as follows:

Anode:

$$4Zn + 8OH^- \rightleftharpoons 4ZnO + 4H_2O + 8e^-$$

Cathode:

$$NO_2^- + 6H_2O + 6e^- \rightarrow NH_3 \cdot H_2O + 7OH^- \text{ (Discharge)}$$

$$CH_3OH + 4OH^- \rightarrow HCOOH + 3H_2O + 4e^- \text{ (Charge)}$$

Overall reactions:

$$4Zn + NO_2^- + 2H_2O + OH^- \rightarrow 4ZnO + NH_3 \cdot H_2O + 2e^- \text{ (Discharge)}$$

$$2ZnO + CH_3OH \rightarrow 2Zn + HCOOH + H_2O \text{ (Charge)}$$

$$NO_2^- + 2CH_3OH + OH^- \rightarrow NH_3 \cdot H_2O + 2HCOOH + 2e^- \text{ (Overall)}$$

Conclusion

In summary, we have successfully synthesized unconventional 2H-phase RhSb alloy NFs for efficient nitrite electroreduction to ammonia. Compared with fcc RhSb NDs and 2H Rh NFs, the as-obtained 2H RhSb NFs demonstrated superior NO_2RR performance in neutral media with the highest NH_3 FE and yield rate of 96.8% and 47.2 mg h^{-1} mg_{cat}^{-1} at −0.3 and −0.6 V (vs. RHE), respectively. Moreover, the as-assembled rechargeable Zn-NO_2^-/MeOH batteries exhibited ultrahigh energy efficiency of 96.4% at 0.1 mA cm^{-2}, excellent long-term cycling durability of 120 h, and potential production of value-added chemicals (NH_3 and HCOOH). Ex/in situ characterizations indicated that 2H RhSb NFs enable kinetically more favorable evolutions for the nitrogen-containing intermediates during NO_2RR. DFT calculations have unraveled that the upshifted Rh-4*d* orbitals in 2H RhSb exhibit higher electroactivity and the surface Sb-5*p* orbitals promote the site-to-site electron transfer. The optimized electronic structure of 2H RhSb is attributed to the stronger interactions between Rh and Sb than that of the *fcc* phase, leading to more efficient reaction trends of NO_2RR. This work not only highlights the importance of phase engineering of alloy nanostructures in improving electrocatalytic performance, but also provides a feasible way of modulating *p–d* orbital coupling strength through phase control.

Acknowledgements

The authors acknowledge the financial support by grants (Project Nos. 22175148 and 52102320) from the National Natural Science Foundation of China, grants (Project Nos. 21309322, 15304023, 15304724, 15307522, N_PolyU502/21, and CRS_PolyU504/22) from the Research Grants Council of Hong Kong, grants (Project Nos. JCYJ20220530140815035 and JCYJ20220531090807017) from the Shenzhen Science and Technology Program, grant (2023A1515012219) from the Natural Science Foundation of Guangdong Province, ITC via the Hong Kong Branch of National Precious Metals Material Engineering Research Center (NPMM), and grants (Project Nos. 9610480, 9610663, 7006007, 7020103, and 9680301) from the City University of Hong Kong. The TEM facility is funded by the Research Grants Council of Hong Kong (Project No. C5029-18E).

Conflict of Interests

The authors declare no conflict of interest.

Data Availability Statement

The data that support the findings of this study are available from the corresponding author upon reasonable request.

Keywords: Alloy nanostructures · Ammonia electrosynthesis · Electrocatalysis · *p–d* Orbital coupling · Phase control

[1] K. K. McLauchlan, J. J. Williams, J. M. Craine, E. S. Jeffers, *Nature* **2013**, *495*, 352–355.
[2] N. Lehnert, B. W. Musselman, L. C. Seefeldt, *Chem. Soc. Rev.* **2021**, *50*, 3640–3646.
[3] X. Zhang, B. B. Ward, D. M. Sigman, *Chem. Rev.* **2020**, *120*, 5308–5351.
[4] Y. Xiong, Y. Wang, J. Zhou, F. Liu, F. Hao, Z. Fan, *Adv. Mater.* **2024**, *36*, 2304021.
[5] V. Hosseininasab, I. M. DiMucci, P. Ghosh, J. A. Bertke, S. Chandrasekharan, C. J. Titus, D. Nordlund, J. H. Freed, K. M. Lancaster, T. H. Warren, *Nat. Chem.* **2022**, *14*, 1265–1269.
[6] Y. Arikawa, Y. Otsubo, H. Fujino, S. Horiuchi, E. Sakuda, K. Umakoshi, *J. Am. Chem. Soc.* **2018**, *140*, 842–847.
[7] S. Kuang, T. Xiao, H. Chi, J. Liu, C. Mu, H. Liu, S. Wang, Y. Yu, T. J. Meyer, S. Zhang, X. Ma, *Angew. Chem. Int. Ed.* **2024**, *63*, e202316772.
[8] E. J. Zakem, A. Al-Haj, M. J. Church, G. L. van Dijken, S. Dutkiewicz, S. Q. Foster, R. W. Fulweiler, M. M. Mills, M. J. Follows, *Nat. Commun.* **2018**, *9*, 1206.
[9] J. Liang, Z. Li, L. Zhang, X. He, Y. Luo, D. Zheng, Y. Wang, T. Li, H. Yan, B. Ying, S. Sun, Q. Liu, M. S. Hamdy, B. Tang, X. Sun, *Chem* **2023**, *9*, 1768–1827.
[10] S. E. Braley, J. Xie, Y. Losovyj, J. M. Smith, *J. Am. Chem. Soc.* **2021**, *143*, 7203–7208.
[11] Y. Wang, Y. Xiong, M. Sun, J. Zhou, F. Hao, Q. Zhang, C. Ye, X. Wang, Z. Xu, Q. Wa, F. Liu, X. Meng, J. Wang, P. Lu, Y. Ma, J. Yin, Y. Zhu, S. Chu, B. Huang, L. Gu, Z. Fan, *Angew. Chem. Int. Ed.* **2024**, *63*, e202402841.
[12] Z. Bi, J. Hu, M. Xu, H. Zhang, Y. Zhou, G. Hu, *Angew. Chem. Int. Ed.* **2024**, *63*, e202313434.
[13] R. Zhang, S. Zhang, Y. Guo, C. Li, J. Liu, Z. Huang, Y. Zhao, Y. Li, C. Zhi, *Energy Environ. Sci.* **2022**, *15*, 3024–3032.
[14] Y. Zhang, Y. Wang, L. Han, S. Wang, T. Cui, Y. Yan, M. Xu, H. Duan, Y. Kuang, X. Sun, *Angew. Chem. Int. Ed.* **2023**, *62*, e202213711.
[15] Y. Hu, J. Liu, C. Lee, W. Luo, J. Dong, Z. Liang, M. Chen, E. Hu, M. Zhang, X. Y. Debbie Soo, Q. Zhu, F. Li, R. S. Rawat, M.-F. Ng, L. Zhong, B. Han, D. Geng, Q. Yan, *ACS Nano* **2023**, *17*, 23637–23648.
[16] J. Lim, Y. Chen, D. A. Cullen, S. W. Lee, T. P. Senftle, M. C. Hatzell, *ACS Catal.* **2023**, *13*, 87–98.
[17] Y. Wang, Y. Xu, C. Cheng, B. Zhang, B. Zhang, Y. Yu, *Angew. Chem. Int. Ed.* **2024**, *63*, e202315109.
[18] N. He, Z. Yuan, C. Wu, S. Xi, J. Xiong, Y. Huang, G. Lian, Z. Du, L. Liu, D. Wu, Z. Chen, W. Tu, Z. Zou, S.-Y. Tong, *ACS Nano* **2025**, *19*, 4684–4693.
[19] Y. Xiong, Y. Wang, C. C. Tsang, J. Zhou, F. Hao, F. Liu, J. Wang, S. Xi, J. Zhao, Z. Fan, *Environ. Sci. Technol.* **2024**, *58*, 10863–10873.
[20] Y. Wang, M. Sun, J. Zhou, Y. Xiong, Q. Zhang, C. Ye, X. Wang, P. Lu, T. Feng, F. Hao, F. Liu, J. Wang, Y. Ma, J. Yin, S. Chu, L. Gu, B. Huang, Z. Fan, *Proc. Natl. Acad. Sci. USA* **2023**, *120*, e2306461120.
[21] H. Xie, Z. Zhao, T. Liu, Y. Wu, C. Lan, W. Jiang, L. Zhu, Y. Wang, D. Yang, Z. Shao, *Nature* **2022**, *612*, 673–678.

[22] Q. Hu, K. Yang, O. Peng, M. Li, L. Ma, S. Huang, Y. Du, Z.-X. Xu, Q. Wang, Z. Chen, M. Yang, K. P. Loh, *J. Am. Chem. Soc.* **2024**, *146*, 668–676.
[23] F. Liu, Z. Fan, *Chem. Soc. Rev.* **2023**, *52*, 1723–1772.
[24] D.-X. Liu, Z. Meng, Y.-F. Zhu, X.-F. Sun, X. Deng, M.-M. Shi, Q. Hao, X. Kang, T.-Y. Dai, H.-X. Zhong, J. Yan, Q. Jiang, *Angew. Chem. Int. Ed.* **2024**, *136*, e202315238.
[25] F. Wang, H. Zhao, G. Zhang, H. Zhang, X. Han, K. Chu, *Adv. Funct. Mater.* **2024**, *34*, 2308072.
[26] Z. Ke, D. He, X. Yan, W. Hu, N. Williams, H. Kang, X. Pan, J. Huang, J. Gu, X. Xiao, *ACS Nano* **2023**, *17*, 3483–3491.
[27] P. Gao, Z.-H. Xue, S.-N. Zhang, D. Xu, G.-Y. Zhai, Q.-Y. Li, J.-S. Chen, X.-H. Li, *Angew. Chem. Int. Ed.* **2021**, *60*, 20711–20716.
[28] Q. Liu, Q. Liu, L. Xie, L. Yue, T. Li, Y. Luo, N. Li, B. Tang, L. Yu, X. Sun, *Chem. Commun.* **2022**, *58*, 5160–5163.
[29] F. Liu, Y. Zou, H. Wang, Z. Wang, M. Zhang, W. Wu, D. Du, W. Zhao, T. Zhao, Y. Liu, N. Yao, Y. Ma, *ACS Nano* **2022**, *16*, 9117–9129.
[30] Z. Fan, M. Bosman, Z. Huang, Y. Chen, C. Ling, L. Wu, Y. A. Akimov, R. Laskowski, B. Chen, P. Ercius, J. Zhang, X. Qi, M. H. Goh, Y. Ge, Z. Zhang, W. Niu, J. Wang, H. Zheng, H. Zhang, *Nat. Commun.* **2020**, *11*, 3293.
[31] Z. Fan, Z. Luo, X. Huang, B. Li, Y. Chen, J. Wang, Y. Hu, H. Zhang, *J. Am. Chem. Soc.* **2016**, *138*, 1414–1419.
[32] Z. Fan, H. Zhang, *Acc. Chem. Res.* **2016**, *49*, 2841–2850.
[33] M. Zhao, Y. Xia, *Nat. Rev. Mater.* **2020**, *5*, 440–459.
[34] Y. Wang, F. Hao, M. Sun, M.-T. Liu, J. Zhou, Y. Xiong, C. Ye, X. Wang, F. Liu, J. Wang, P. Lu, Y. Ma, J. Yin, H.-C. Chen, Q. Zhang, L. Gu, H. M. Chen, B. Huang, Z. Fan, *Adv. Mater.* **2024**, *36*, 2313548.
[35] Y. Ma, M. Sun, H. Xu, Q. Zhang, J. Lv, W. Guo, F. Hao, W. Cui, Y. Wang, J. Yin, H. Wen, P. Lu, G. Wang, J. Zhou, J. Yu, C. Ye, L. Gan, D. Zhang, S. Chu, L. Gu, M. Shao, B. Huang, Z. Fan, *Adv. Mater.* **2024**, *36*, 2402979.
[36] F. Liu, Y. Zou, X. Tang, L. Mao, D. Du, H. Wang, M. Zhang, Z. Wang, N. Yao, W. Zhao, M. Bai, T. Zhao, Y. Liu, Y. Ma, *Adv. Funct. Mater.* **2022**, *32*, 2204601.
[37] J.-Y. Fang, Q.-Z. Zheng, Y.-Y. Lou, K.-M. Zhao, S.-N. Hu, G. Li, O. Akdim, X.-Y. Huang, S.-G. Sun, *Nat. Commun.* **2022**, *13*, 7899.
[38] Z. Huang, B. Yang, Y. Zhou, W. Luo, G. Chen, M. Liu, X. Liu, R. Ma, N. Zhang, *ACS Nano* **2023**, *17*, 25091–25100.
[39] F. Liu, J. Zhou, Y. Wang, Y. Xiong, F. Hao, Y. Ma, P. Lu, J. Wang, J. Yin, G. Wang, J. Yu, Y. Yan, Z. Zhu, J. Zeng, Z. Fan, *Small Struct.* **2023**, *4*, 2300025.
[40] C. Chang, W. Chen, Y. Chen, Y. Chen, Y. Chen, F. Ding, C. Fan, H. J. Fan, Z. Fan, C. Gong, Y. Gong, Q. He, X. Hong, S. Hu, W. Hu, W. Huang, Y. Huang, W. Ji, D. Li, L.-J. Li, Q. Li, L. Lin, C. Ling, M. Liu, N. Liu, Z. Liu, K. P. Loh, J. Ma, F. Miao, H. Peng, et al., *Acta Phys. Chim. Sin.* **2021**, *37*, 2108017.
[41] Q. Gao, B. Yao, H. S. Pillai, W. Zang, X. Han, Y. Liu, S.-W. Yu, Z. Yan, B. Min, S. Zhang, H. Zhou, L. Ma, H. Xin, Q. He, H. Zhu, *Nat. Synth.* **2023**, *2*, 624–634.
[42] K. Liu, H. Li, M. Xie, P. Wang, Z. Jin, Y. Liu, M. Zhou, P. Li, G. Yu, *J. Am. Chem. Soc.* **2024**, *146*, 7779–7790.
[43] E. Murphy, Y. Liu, I. Matanovic, M. Rüscher, Y. Huang, A. Ly, S. Guo, W. Zang, X. Yan, A. Martini, J. Timoshenko, B. R. Cuenya, I. V. Zenyuk, X. Pan, E. D. Spoerke, P. Atanassov, *Nat. Commun.* **2023**, *14*, 4554.
[44] J. Xu, S. Zhang, H. Liu, S. Liu, Y. Yuan, Y. Meng, M. Wang, C. Shen, Q. Peng, J. Chen, X. Wang, L. Song, K. Li, W. Chen, *Angew. Chem. Int. Ed.* **2023**, *62*, e202308044.
[45] Q. Yao, Z. Yu, L. Li, X. Huang, *Chem. Rev.* **2023**, *123*, 9676–9717.
[46] Z. Zhang, G. Liu, X. Cui, Y. Gong, D. Yi, Q. Zhang, C. Zhu, F. Saleem, B. Chen, Z. Lai, Q. Yun, H. Cheng, Z. Huang, Y. Peng, Z. Fan, B. Li, W. Dai, W. Chen, Y. Du, L. Ma, C.-J. Sun, I. Hwang, S. Chen, L. Song, F. Ding, L. Gu, Y. Zhu, H. Zhang, *Sci. Adv.* **2021**, *7*, eabd6647.
[47] Q. N. Nguyen, E. M. Kim, Y. Ding, A. Janssen, C. Wang, K. K. Li, J. Kim, K. A. Fichthorn, Y. Xia, *J. Am. Chem. Soc.* **2024**, *146*, 12040–12052.
[48] X. Huang, B. Xu, J. Feng, S. Hu, W. Dou, T. Yang, C. Zhan, S. Liu, Y. Ji, Y. Li, C.-W. Pao, Z. Hu, Q. Shao, X. Huang, *J. Am. Chem. Soc.* **2023**, *145*, 28010–28021.
[49] Z. Li, L. Zhai, Q. Zhang, W. Zhai, P. Li, B. Chen, C. Chen, Y. Yao, Y. Ge, H. Yang, P. Qiao, J. Kang, Z. Shi, A. Zhang, H. Wang, J. Liang, J. Liu, Z. Guan, L. Liao, V. A. Neacşu, C. Ma, Y. Chen, Y. Zhu, C.-S. Lee, L. Ma, Y. Du, L. Gu, J.-F. Li, Z.-Q. Tian, F. Ding, et al., *Nat. Mater.* **2024**, *23*, 1355–1362.
[50] K. Liu, H. Yang, Y. Jiang, Z. Liu, S. Zhang, Z. Zhang, Z. Qiao, Y. Lu, T. Cheng, O. Terasaki, Q. Zhang, C. Gao, *Nat. Commun.* **2023**, *14*, 2424.
[51] J. Zhou, Z. Xu, K. Cui, J.-A. Yin, H.-C. Chen, Y. Wang, F. Liu, T. Wang, F. Hao, Y. Xiong, C. Wang, Y. Ma, P. Lu, J. Yin, L. Guo, X. Meng, C. Ye, H. M. Chen, Y. Zhu, J. Lu, Z. Fan, *Angew. Chem. Int. Ed.* **2025**, *64*, e202416947.
[52] N. He, S. Wu, W. Yu, F. Jin, W. Xie, X. Lu, X. Zhao, Z. Chen, W. Tu, S. Y. Tong, *Sci. China Mater.* **2025**, *68*, 180–188.
[53] K. Chen, Z. Ma, X. Li, J. Kang, D. Ma, K. Chu, *Adv. Funct. Mater.* **2023**, *33*, 2209890.
[54] M. Xie, S. Tang, Z. Li, M. Wang, Z. Jin, P. Li, X. Zhan, H. Zhou, G. Yu, *J. Am. Chem. Soc.* **2023**, *145*, 13957–13967.
[55] G. Wu, W. Zhang, R. Yu, Y. Yang, J. Jiang, M. Sun, A. Du, W. He, L. Dai, X. Mao, Z. Chen, Q. Qin, *Angew. Chem. Int. Ed.* **2024**, *136*, e202410251.
[56] S.-L. Meng, C. Zhang, C. Ye, J.-H. Li, S. Zhou, L. Zhu, X.-B. Li, C.-H. Tung, L.-Z. Wu, *Energy Environ. Sci.* **2023**, *16*, 1590–1596.
[57] S. Liu, L. Cui, S. Yin, H. Ren, Z. Wang, Y. Xu, X. Li, L. Wang, H. Wang, *Appl. Catal. B* **2022**, *319*, 121876.
[58] C. Wang, W. Zhou, Z. Sun, Y. Wang, B. Zhang, Y. Yu, *J. Mater. Chem. A* **2021**, *9*, 239–243.
[59] L. Ouyang, X. He, S. Sun, Y. Luo, D. Zheng, J. Chen, Y. Li, Y. Lin, Q. Liu, A. M. Asiri, *J. Mater. Chem. A* **2022**, *10*, 23494–23498.
[60] L. Yi, P. Shao, H. Li, M. Zhang, X. Peng, K. Chen, X. Liu, Z. Wen, *J. Power Sources* **2023**, *559*, 232668.
[61] P. Gao, Z. H. Xue, S. N. Zhang, D. Xu, G. Y. Zhai, Q. Y. Li, J. S. Chen, X. H. Li, *Angew. Chem. Int. Ed.* **2021**, *60*, 20711–20716.
[62] L. Ouyang, X. Fan, Z. Li, X. He, S. Sun, Z. Cai, Y. Luo, D. Zheng, B. Ying, J. Zhang, *Chem. Commun.* **2023**, *59*, 1625–1628.
[63] L. Hu, D. Zhao, C. Liu, Y. Liang, D. Zheng, S. Sun, Q. Li, Q. Liu, Y. Luo, Y. Liao, *Inorg. Chem. Front.* **2022**, *9*, 6075–6079.
[64] J. Zhou, Y. Xiong, M. Sun, Z. Xu, Y. Wang, P. Lu, F. Liu, F. Hao, T. Feng, Y. Ma, J. Yin, C. Ye, B. Chen, S. Xi, Y. Zhu, B. Huang, Z. Fan, *Proc. Natl. Acad. Sci. USA* **2023**, *120*, e2311149120.
[65] R. Zhang, Y. Guo, S. Zhang, D. Chen, Y. Zhao, Z. Huang, L. Ma, P. Li, Q. Yang, G. Liang, C. Zhi, *Adv. Energy Mater.* **2022**, *12*, 2103872.
[66] Y. Guo, R. Zhang, S. Zhang, Y. Zhao, Q. Yang, Z. Huang, B. Dong, C. Zhi, *Energy Environ. Sci.* **2021**, *14*, 3938–3944.

Manuscript received: February 26, 2025
Revised manuscript received: March 26, 2025
Accepted manuscript online: April 02, 2025
Version of record online: April 11, 2025